Ultramicroscopy 242 (2022) 113624

Contents lists available at ScienceDirect

Ultramicroscopy

journal homepage: www.elsevier.com/locate/ultramic

Tunable magnetic field source for magnetic field imaging microscopy

Andris Berzins [a,*], Hugo Grube [a], Reinis Lazda [a], Marc A. Hannig [b,a], Janis Smits [c,a], Ilja Fescenko [a]

[a] Laser Centre, University of Latvia, Jelgavas Street 3, LV-1004 Riga, Latvia
[b] Faculty of Mathematics and Physics, Leibniz University Hannover, 30167 Hannover, Germany
[c] The University of New Mexico, Albuquerque, United States

ARTICLE INFO

Keywords:
Magnetic field imaging microscopy
Tunable magnetic field source
Nitrogen–Vacancy centers
Optically detected magnetic resonance

ABSTRACT

In this work, we present a novel, compact, power efficient and variable magnetic field source design for magnetic field imaging microscopy. The device is based on a pair of diametrically magnetized permanent magnet cylinders with electro-mechanical rotation control and ferrite flux homogenizers. A Hall probe and NV centers in diamond are used to demonstrate a proof of concept of a proposed magnetic field setup and to characterize the homogeneity of the produced magnetic field on a micrometer scale. Numerical simulation results are compared with experimental results showing good agreement of the distribution of the magnetic field in the setup. As a result, a magnetic field source with a tunable field amplitude in the range from 1 mT to 222 mT is demonstrated, achieving a magnetic field homogeneity of 2 ppm/μm or 0.5 μT/μm at 222 mT in a 25 × 25 μm field of view.

1. Introduction

Nitrogen–Vacancy (NV) centers in diamond [1] have demonstrated themselves as a useful platform for magnetic field microscopy, that can be used to reveal two dimensional magnetic structures of various samples: magnetic mapping of superconducting thin films [2,3] and microscopic electromagnetic devices [4–6], as well as imaging of micrometer and nanometer sized particles [7,8], thin film structures [9–12], nanoscale magnetic resonance [13], magnetic spins [14] and eddy currents [15] to name a few. Furthermore, it is evident that NV based microscopy is well suited for the investigation of wide range temperature dependent magnetic effects on a microscopic scale as well [2,16,17].

In many cases relatively strong and variable magnetic fields are favored to reach the material's magnetic saturation in case of paramagnetic or superparamagnetic materials [7,11], or to reach the anti-crossing regions of the NV centers [18]. However, the devices that can reach the few hundred mT fields often are electromagnets that are bulky, require either high voltage or high currents delivered with high accuracy, and are relatively expensive to make and exploit, as well as are prone to heating. There are also various sophisticated permanent magnet designs that allows to change and control the magnetic field in two or three dimensions as well as to create multi-pole fields, like nested Halbach cylinders [19–23], combinations of multiple rotating magnets cylinders (Halbach design) [24–28], permanent magnet arrays [29], as well as shifting yokes [30,31] to name a few. However, these devices still have relatively complex designs with the need to precisely orient from four to few tens of magnets. This complexity is not always necessary for microscopy measurements that focus on two-dimensional layer on scale of 100 × 100 μm and measurement depth of around 1 μm (very common in studies related to the NV centers).

With this research we present a blueprint for a simple, compact, inexpensive, and easy-to-customize solution for a variable magnetic field source for magnetic field imaging microscopy using NV centers in diamond that is based on two rotatable permanent magnets. In order to increase the homogeneity of the magnetic field, ferrite magnetic flux homogenizers are placed between the two permanent magnets. The magnetic flux homogenizers improve the magnetic field homogeneity and amend any small misalignment of the permanent magnets. As a result, our setup delivers magnetic fields up to 222 mT with a magnetic field homogeneity of down to 2 ppm/μm. Our setup can deliver bias magnetic field in micro-scale with much smaller gradients than can be acquired by using single permanent magnet sources, while having comparable magnetic field homogeneity with other more complicated devices [19,28]. At the same time this setup delivers larger amplitude magnetic field than can be achieved by electromagnets of similar size. Although this device is demonstrated using NV centers, it can be used for other applications as well, as the compact design allows it to be combined with commercial microscopes, while the gap in the middle of presented device allows it to be fitted around commercial microscope objectives.

Using such a setup allows for changes from a close to zero magnetic field to a relatively high magnetic field by rotating both permanent

* Corresponding author.
E-mail address: andris.berzins@lu.lv (A. Berzins).

https://doi.org/10.1016/j.ultramic.2022.113624
Received 31 December 2021; Received in revised form 21 July 2022; Accepted 24 September 2022
Available online 30 September 2022

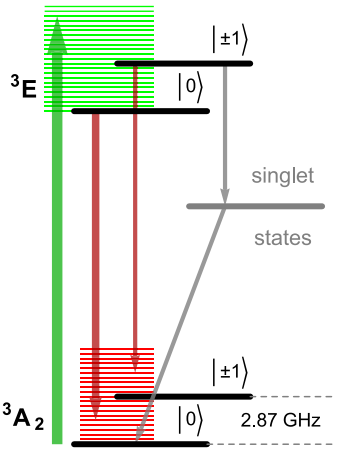

Fig. 1. NV energy level diagram depicting magnetic sublevels ($|0\rangle$, $|\pm1\rangle$), their phonon bands (green and red horizontal lines), optical excitation (green arrow), fluorescence (red arrows), and nonradiative (gray arrows) pathways. Gray arrows show spin-selective intersystem crossing leading to polarization into the $|0\rangle$ ground-state sublevel.

magnets around their main cylindrical axes. Such a mode of operation gives a useful tool for hysteresis measurements, that usually require a combination of relatively large magnetic fields with the possibility to gradually increase or decrease the magnetic field, as well as change the field direction [32–35].

2. Experimental methods

To determine the uniformity of the magnetic field on micro-scale in the volume between the two permanent magnets we made Hall probe (SENIS F3 A with sensor size of 0.03 × 0.005 × 0.03 mm^3 used for By measurements) and NV based measurements of the spatial distribution of Optically Detected Magnetic Resonance (ODMR) [36] on a diamond placed in between the magnet system.

The NV energy levels with optical excitation and emission pathways are depicted in Fig. 1. When green laser light (532 nm) continuously excites NV centers, the ground-state population is optically polarized into the $|0\rangle$ state by a non-radiative, spin-selective decay via intermediate singlet states. Because of this spin-selective decay mechanism, NV centers excited from the $|0\rangle$ state emit fluorescence in the red region of the spectrum at a higher rate than those originating from $|\pm1\rangle$ states. Application of a microwave (MW) field mixes the spin populations, resulting in a decrease in the fluorescence when the MW frequency matches the spin transition frequencies, $f_{\pm}$. Evaluation of these frequencies by precisely measuring the NV fluorescence as the MW frequency is swept across the resonances is the basic principle of ODMR techniques.

As the luminescence signal was collected and detected using an optical system, that maintains the two-dimensional information of the luminescence distribution of the NV layer in the diamond, the magnetic field distribution over the field of view could be reconstructed after data processing (described in next section).

3. Experimental setup

The experimental setup consists of two main parts: the optical system to guide the exciting green laser light to the diamond sample and afterwards gather the red fluorescence from the NV centers in the diamond and guide it to a photodiode or a camera, and the electro-mechanical system for applying magnetic field by controlling the rotation angle of the two cylindrical permanent magnets. The setup for widefield magnetic field imaging with the system for the application of a bias magnetic field is depicted in Fig. 2.

The diamond we used as the magnetic field probe is an HPHT diamond with dimensions 2.0 × 2.0 × 0.06 mm and (110) surface polish. We performed **S**topping **R**ange of **I**ons in **M**atter or SRIM simulations [37] to determine the implantation parameters required for the fabrication of a 200-nm-thick NV layer close to the diamond surface. The crystal was irradiated with ^{4}He ions at three separate energies and doses: 6.0 × 10^{12} He/cm^2 at 5 keV, 6.0 × 10^{12} He/cm^2 at 15 keV, and 1.20 × 6.0 × 10^{13} He/cm^2 at 33 keV. After that the diamond was annealed for four hours at 800 °C and for four hours at 1100 °C under high vacuum to promote migration of vacancies to the substitutional nitrogen defects, as well as to allow the crystal to heal after irradiation.

The diamond is placed on a coverslip that is attached to a sample holder, that in turn is attached to a 3 axis translation stage enabling the sample movement and focus adjustment in an epifluorescent microscope. The NV excitation and fluorescence detection is performed through the same infinity-corrected 100× microscope objective with a numerical aperture of 1.25 (100x/1.25 Oil, ∞/0.17, ZEISS). The NV centers are exposed to 200 mW of green radiation guided by a multimode optical fiber and lens system from a Coherent Verdi V-18 laser. The NV fluorescence (650–800 nm) is separated from the green light by a dichroic mirror (Thorlabs DMLP567R) and imaged through a long-pass filter (Thorlabs FEL0600) on a sCMOS sensor of an Andor Neo 5.5 camera, or on a photodiode (Thorlabs PDA36A-EC). The field of view detected by the Andor camera detector region of 512 × 512 pixels during measurements is an area of about 25 × 25 μm^2. The diffraction-limited spatial resolution defined by the NA of the microscope objective sets the fundamental limit of resolution ~350 nm, that is reduced by the air gap between the coverslip and the diamond to an estimate of ~700 nm.

The MW field, necessary for the ODMR measurements, is produced by a SRS SG386 generator. The MW frequency is slowly swept using the analog voltage of a sawtooth waveform, which is delivered from a data acquisition card (NI USB-6001). The amplified MW field (Mini Circuits ZVE-3W-83+ or ZVE-3W-183+ amplifier) is delivered to the diamond by a copper wire with a diameter of 50 μm. To reach some of the necessary frequency regions we also used a frequency doubler Mini Circuits ZX90-2-24-S+. The MW frequency is swept across a central frequency of an ODMR ($|0\rangle \leftrightarrow |+1\rangle$ or $|-1\rangle$ transition) profile with a deviation of ±15 MHz. The MW sweep is triggered by a pulse from the sCMOS camera, which records 40 frames per sweep. The acquisition time of one frame (512 × 512 pixels) is 7 to 9 ms (depending on the set exposure time). Five series of frames are averaged in the camera memory before being read out by a LabVIEW interface. Typically, for magnetic field gradient measurements we averaged about 3000 measurements. As a result, we obtained NV fluorescence images that reveal an ODMR shape for each pixel. In post-processing, we fit the obtained ODMR profiles pixel-wise with a Lorentzian function to obtain a two-dimensional map of the ODMR central frequencies for both $|0\rangle \leftrightarrow |+1\rangle$ and $|-1\rangle$ transitions separately. After that, the obtained values for each transition for each corresponding pixel is subtracted from each other, the results can then be interpreted as magnetic field values. In this way a magnetic field image is constructed.

The magnets used for this setup are custom made diametrically magnetized (the magnetization vector is perpendicular to the principal cylindrical axis of the magnets) N50 magnet cylinders (from NINGBO ZHAOBAO MAGNET CO., LTD.), 30 mm in height and 50 mm in diameter. There is a 44 mm gap between the outer edges of the permanent magnets. The magnets are fixed in space so that the distance between them cannot change, but their mounts allow them to spin around their respective main cylindrical axes. The magnetic flux homogenizers 30 mm × 50 mm × 5 mm made of ferrite MN60 (The National Magnetics Group. Inc.) are placed at a distance of 4 mm from the outer edges of the permanent magnets (with their longer edge in the direction of the permanent magnet cylindrical axis) leaving a free space of 26 mm between the ferrite flux homogenizers, where the diamond sensor is

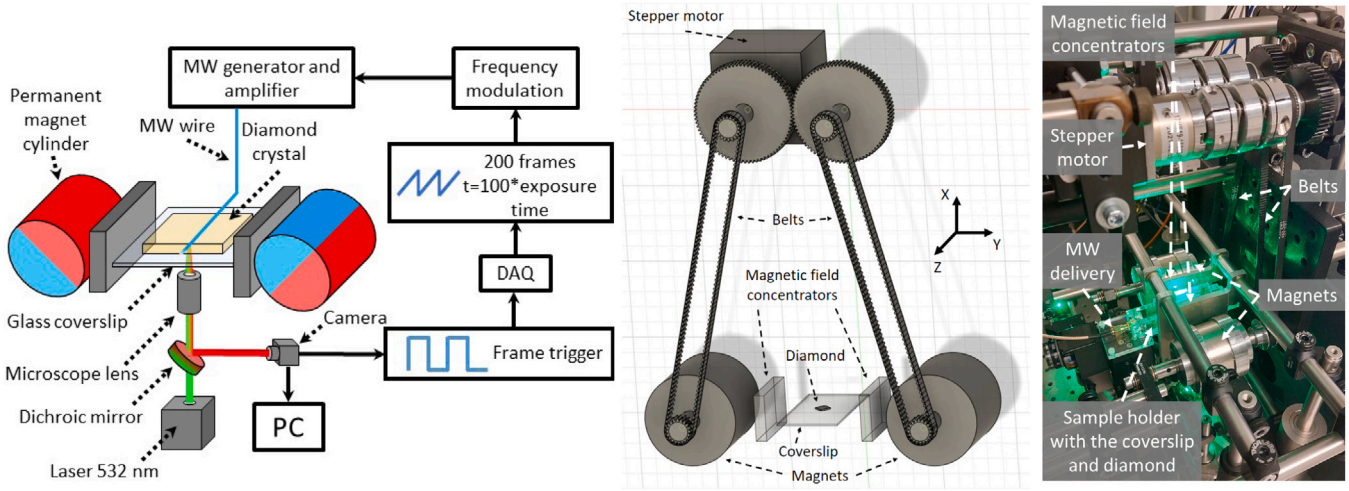

Fig. 2. **Left**: Schematic of the experimental apparatus for widefield diamond microscopy, DAQ: data acquisition card; PC: personal computer. **Middle**: 3D model of the permanent magnet rotation mechanism. **Right**: The magnet setup in the laboratory. The ferrite flux homogenizers are held in place by custom made aluminum holders, the coverslip with the diamond is placed between the magnetic flux homogenizers by a custom made sample holder.

placed at the center point between the permanent magnets, where the magnetic field produced by this system is the most homogeneous, see Fig. 2. The material chosen for the ferrite flux homogenizers was MN60 (soft ferrite) due to the very low hysteresis or remnant magnetization after the external field is removed (on the order of nT). MN60 also has very low magnetization noise vs relative loss factor, and very low thermal magnetic noise [38]. We did not use hard ferrites that would saturate at much higher magnetic field (providing better field concentration), as the pronounced hysteresis would make the operation at low magnetic fields very challenging and prone to remnant magnetization set bias fields.

To diminish the magnetic field gradient that the diamond sensor could be exposed to, the magnet system is placed around the diamond in a way that the principal cylindrical axis of the magnets are parallel to the plane of the coverslip, see Fig. 2. In this way only the 200 nm thin NV layer in the diamond is sensing the magnetic field gradient that is more pronounced in the direction perpendicular to the diamond surface (see Fig. 3). And, as the magnetic field lines have a relatively large curvature radius, it can be considered that within the field-of-view and the depth of NV layer (200 nm) the magnetic field is relatively homogeneous. It has to be noted that a situation where the principal cylindrical axis of the magnets are perpendicular to the plane of the coverslip might seem to be very similar, but in practice it is not so, the reason is clearly visible in Fig. 3(b) where the gradients along the **Y** axis is much less pronounced than along the **X** axis.

The permanent magnet system is aligned and controlled in the following way: the rotation (the angular position) of the magnets is controlled by a stepper motor with a reduction unit (resulting in 54 920 steps per revolution) controlled by a custom software. The stepper motor drives a shaft which is connected to another separate shaft via two equal spur gears, ensuring that the two shafts rotate in the opposite directions (Fig. 2 middle). This is necessary to enable the system to reach the two extreme points: (1) to reach the maximum magnetic field, magnet poles are aligned with the **Y** axis and face in the same direction, (2) to reach the minimum value of the magnetic field, magnet poles are aligned with the **X** axis and face in the opposite directions. Such a system also makes it possible to achieve all intermediate values of the magnetic field between the two extreme cases. Further on, this stepper motor, shaft, and gear aggregate is connected to the constructions holding the magnet cylinders themselves via a timing pulley and timing belt system. The magnetic field produced in between the two magnets can then be easily aligned with one of the NV axes in the diamond which is surface polished along the (110) direction.

Such a system has several benefits: gear system that allows simultaneous rotation control of both magnet cylinders by using only one stepper motor; timing belts allow to position the stepper motor relatively far from the center of the experimental system (in our case ≈20 cm away from the magnets); the reduction unit allows for very precise control of the angle of the magnets and allows the use of relatively weak stepper motors. The COMSOL simulations show that maximum torque experienced by the magnet cylinder is 0.1 Nm and 0.16 Nm is experienced by each ferrite; the maximum force experienced by each magnet cylinder is 17 N and 40 N is experienced by each ferrite.

The diamond sample is placed in the free space gap in between the ferrite flux homogenizers at the center point between the two permanent magnets. The diamond is held in place on a coverslip by a copper wire used for the MW delivery. The wire is tensioned in order for it to lightly press the diamond against the coverslip to hold it in place (still allowing for some rotation of the diamond for alignment purposes) as well as to ensure the minimal possible distance between the wire and the NV layer. The magnetic field images obtained using this experimental setup are used to determine the uniformity of the magnetic field between the two permanent magnets.

4. Results

To characterize the homogeneity of the magnetic field at the center between the two permanent magnets with the magnetic flux homogenizers, we first did magnetic field simulations by using the **F**inite **E**lement **M**ethod **M**agnetics or FEMM simulation software (Fig. 3) and COMSOL simulations (Fig. 4) for three separate cases:

- **(A)** both the magnetization directions are facing in the same direction (→ →) along the **Y** direction, producing the maximum possible magnetic field (Fig. 3(a)),
- **(B)** the magnetization directions both make a 45° angle with respect to the **Y** direction (↘ ↗), producing an intermediate magnetic field value (Fig. 3(b)),
- **(C)** the magnetization directions are opposite to one another (↓ ↑) along the **X** direction, producing a minimum magnetic field (Fig. 3(c)).

Numerical simulations from FEMM (Fig. 3) show that at the center between the magnets a gradient along the **X** axis exists in all cases except when the magnets produce a close to zero magnetic field or are aligned for the maximum magnetic field. However, gradients along the **Y** axis are much lower. To clearly demonstrate the difference between

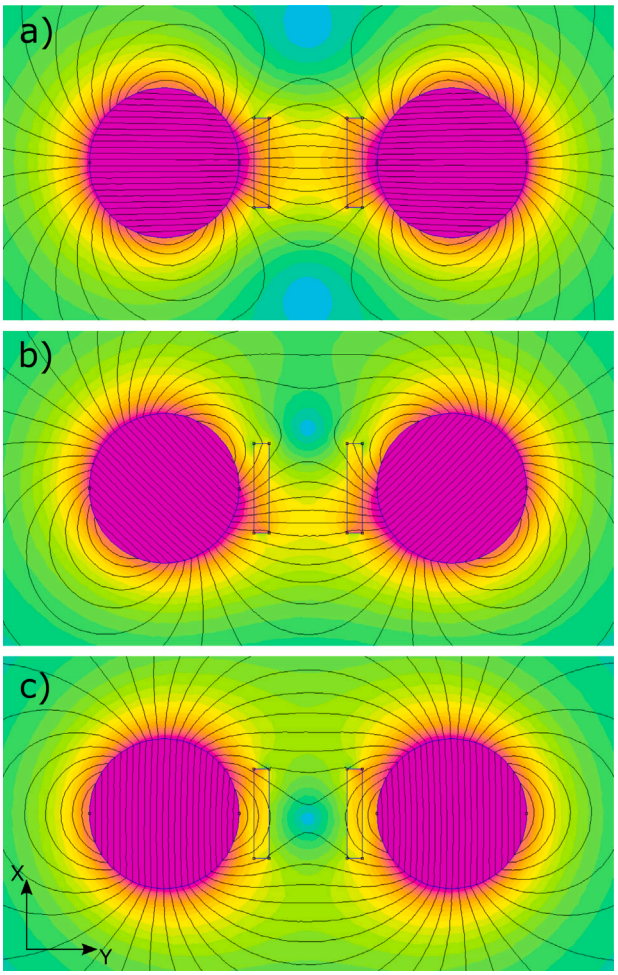

Fig. 3. A 2D magnetic field density plot. Simulation performed using a finite element simulation software (FEMM) showing the two permanent magnets with the ferrite flux homogenizers between them. Color coding represents the |B| with cyan color representing low magnetic field, and red and pink color representing high magnetic field. Black lines represent the magnetic field lines. The observation for this simulation is done in the direction of the magnets cylindrical axis, this allows to see a magnetic field gradient in the **X** direction between the magnets for multiple magnetic field configurations. Due to this gradient, the coverslip with the diamond is placed along the **YZ** plane, and perpendicular to the **X** direction (as shown in Fig. 2). The configurations of the two permanent magnets used in the simulations are: (a) → →, (b) ↘ ↗, (c) ↓ ↑.

the magnet systems with and without flux homogenizers and to analyze the magnetic field in the center of the magnet system along the **Y** axis (axis that is expected to give the largest gradient value in YZ plane) we made measurements using a Hall probe on a positioning platform (allowing a 4 mm travel range) and made COMSOL simulations for cases **(A)**, **(B)** and **(C)** (Fig. 4).

Firstly, experimentally measured results, using a Hall magnetic field probe, compared to the magnetic field distribution simulations (Fig. 4(a)–(b)), show good agreement between the experiment and the predicted behavior of the magnet system from the simulations. In this case the maximum deviation between the measurement and simulation reached 24.5 mT or about 10%.

Secondly, measurements and simulations show the benefit of having the flux homogenizers in all cases (Fig. 4(a)–(b), simulations and measurements denoted as WF or With Ferrites versus simulations and measurements denoted as NF or No Ferrites). The flux homogenizers straighten out the magnetic field lines with respect to the coverslip/diamond plane, lessening the magnetic field gradient in the **Y** direction. Besides, flux homogenizers compensate for small deviations from the perfect geometry of the magnet position (pitch, roll or imperfections of angular rotation of one magnet with respect to the other), that can easily occur in real-life systems.

Thirdly, Fig. 4(d)–(f) present the derivative of the data obtained by the COMSOL simulations, giving the magnetic field gradient per μm for each magnet orientation. Again, the benefit of having the flux homogenizers (results denoted as WF) is clearly visible, yielding a gradient with roughly twice as less amplitude compared to the case without flux homogenizers (results denoted as NF).

To test the experimental set-up on the micro scale we performed ODMR measurements in two measurement modes: measuring the ODMR signal with a photodiode for magnetic fields up to 100 mT, and magnetic field imaging measurements for three magnetization directions **(A)**, **(B)** denoted in the start of this chapter and a configuration producing a magnetic field of 28 mT. The results from the measurements with a photodiode are depicted in Fig. 5, giving the average ODMR value over the illumination region of ≈30 μm × 30 μm for a range of magnetic field values.

One of the things that can be seen in Fig. 5 is that at the minimum magnetic field value the ODMR profile is still split, meaning that the magnetic field is not zero, it is estimated to be approximately 0.95 mT. Another feature that can be seen from Fig. 5 is that at low magnetic fields (up to 40 mT) the bias magnetic field is not perfectly aligned with one of the NV axis, as the resonances created by the NV centers that are not aligned with the magnetic field are split in two. This occurs simply due to the fact that the fine tuning of the diamond orientation was done at ≈70 mT. A coarse alignment was done by rotating the diamond on the surface of the coverslip and fine adjustments were done by slightly changing the angle of the magnetic flux homogenizers in order to compensate for any magnetic field in the vertical direction (**X** axis) with respect to the diamond. A small misalignment of the bias field occurs due to the laboratory fields that change when the magnets are rotated (mainly because of the microscope objective and its holder, that are not completely nonmagnetic).

To determine the spatial distribution of the magnetic field gradient on a micro scale we performed magnetic field imaging measurements for the three magnet pair configurations: **(A)** producing a 222 mT field, **(B)** producing a 164 mT field denoted in the start of this chapter and a configuration producing a 28 mT field as zero and close to zero magnetic fields cannot be measured by the method we are using. It has to be noted that the maximum magnetic field value is a bit different than in measurements with the Hall probe because the distance between the flux homogenizers was slightly changed. The obtained results can be seen in Fig. 6. In all measurements the results are depicted in the following way: the data in each row represents one measurement set at the magnetic field value denoted at the left side of the row; columns (a) and (b) represent the ODMR maps obtained for separately measured transitions $|0\rangle \leftrightarrow |+1\rangle$ and $|-1\rangle$; column (c) presents the obtained magnetic field maps; (d) presents the total fluorescence distribution normalized to the maximum value of the fluorescence over the field of view.

The ODMR maps in columns (a) and (b) in Fig. 6 present the resonance frequency maps, where the ODMR frequencies are given a color coding for creation of 2D maps. In the case of Fig. 6 measurements at 28 mT, the ODMR gradients in (1) and (4) present a shift in opposite directions, but in measurements at 164 mT (2) and (5) and at 222 mT (3) and (6) the frequency shifts have the same overall shape. This is expected and can be easily explained with the bias magnetic field in perspective of the NV center energy scheme: in the case of Fig. 6(1) and (4) the measurements are done at frequencies that are well below the GSLAC [39], meaning that by increasing the magnetic field the transition $|0\rangle \longrightarrow |-1\rangle$ moves towards lower frequencies, but $|0\rangle \longrightarrow |+1\rangle$ moves towards higher frequencies. However, in the cases of Fig. 6(2) and (5), and Fig. 6(3) and (6), the central ODMR frequencies are above the GSLAC, and thus by increasing or decreasing

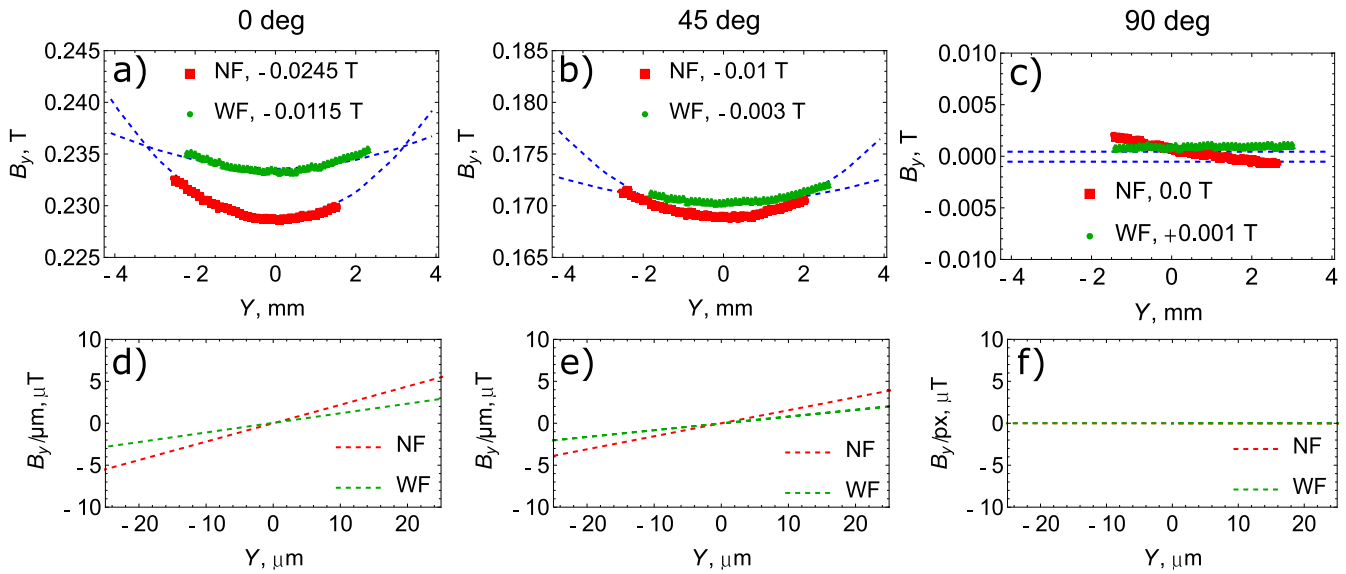

Fig. 4. Simulations and measurements done by a Hall probe. These line plots show the magnetic field distribution along the **Y** direction between the two magnets for three different configurations of the two permanent magnets: (a) → →, (b) ↘ ↗, (c) ↓ ↑. Case with flux homogenizers denoted as **WF** or With Ferrites versus case without flux homogenizers denoted as **NF** or No Ferrites. The magnetic field derivative (gradient per μm) at the center of the device simulated in COMSOL environment for three different configurations of the two permanent magnets (d) → →, (e) ↘ ↗, (f) ↓ ↑.

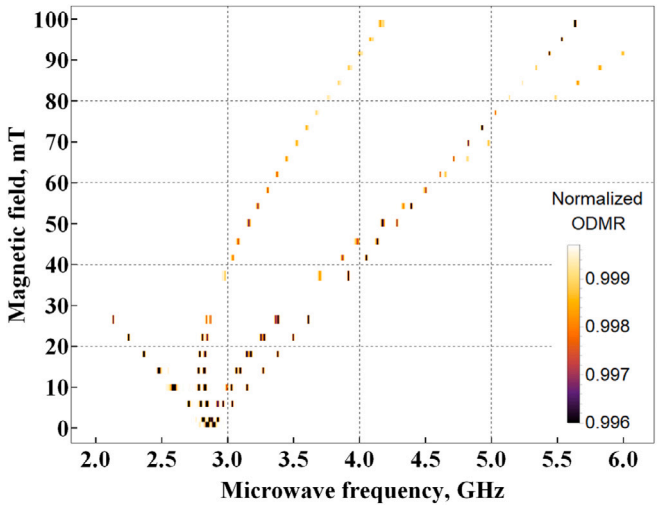

Fig. 5. ODMR from the NV centers giving the average ODMR frequency value over the illumination region of ≈30 μm × 30 μm^2. The permanent magnet rotation angles were changed from 0° to 24° resulting in a magnetic field change from close to zero to 100 mT. The ODMR measurements were done keeping the three ODMR signal components that are not aligned with the magnetic field in the MW scan range to see how they change depending on the magnet angle, how good they are overlapping.

the magnetic field, both transitions experience frequency shifts in the same positive or negative direction.

The magnetic field maps (column c) in Fig. 6 are obtained in the following way, first, the two corresponding ODMR maps are subtracted from each other (or added in the cases where the magnetic field is above 102.4 mT). This is done to get rid of signals that could potentially occur due to strain and temperature related effects, as these effects shift both resonance frequencies in the same direction, while magnetic field related effects shift the resonances in the opposite directions. After the subtraction, the obtained frequencies are divided by 28.025, as the transition frequency for the NV centers aligned with the magnetic field is linear and changes by 28.025 MHz/mT. After that the 2D magnetic field map is given color coding. For in depth analysis we also constructed line plots representing the magnetic field gradients, see Fig. 8. The results obtained give a convenient mode of assessment of the field gradient over the field of view, as well as gradient determination over one camera pixel. These line plots representing the magnetic field gradients are constructed in the following way, both profiles Y and Z are constructed by taking data from the middle part of the magnetic field profiles presented in column (c) of Fig. 6. To lessen the impact of the noise we averaged 30 adjacent pixel rows for Z profile, and 30 adjacent columns for Y profile (the analysis of the noise structure can be found in the Appendix). The straight lines are linear fits of the data, the slope values give the change in magnetic field per μm for each direction. One would expect that larger bias magnetic fields create larger magnetic field gradients (in the means of amplitude), however in our case the magnetic field gradient in the **Y** direction is largest at 28 mT and smallest at 164 mT. The magnetic field gradient in the **Z** direction is very low at 28 mT and is the highest at 164 mT. There are two main reasons for varying magnetic field gradient amplitudes, first, the way how we fine-tune the magnetic field direction relative to the diamond is by making small adjustments to the concentrator pair angle, thus this potentially can move the magnetic center of the set-up. In other words, looking at Fig. 4 non-zero field cases, the concentrator pair adjustments move the measurement spot to the left or right of the center (0 mm) position, meaning that the measurements are not done at the bottom of the U-shape, but on one of the sides, resulting in a larger gradient. Second, as the microscope objective and its holder, are not completely nonmagnetic, and, by rotating the magnets, these parts experience and generate some magnetic field of their own, thus slightly changing the direction of the total field felt by the diamond. And it is expected, that these small deviations have a larger effect at smaller bias fields when small perturbations have a more noticeable effect on the general direction of the magnetic field.

To give another perspective on the obtained results we estimated the impact of a magnetic field gradient on the FWHM of the ODMR profile within one detection pixel of the magnetic microscope. Here we assumed that the average size of the detection pixel is 0.5 × 0.5 μm^2. Based on this one can estimate the maximal magnetic field gradients acceptable for optimal magnetic field imaging measurements, see Fig. 7.

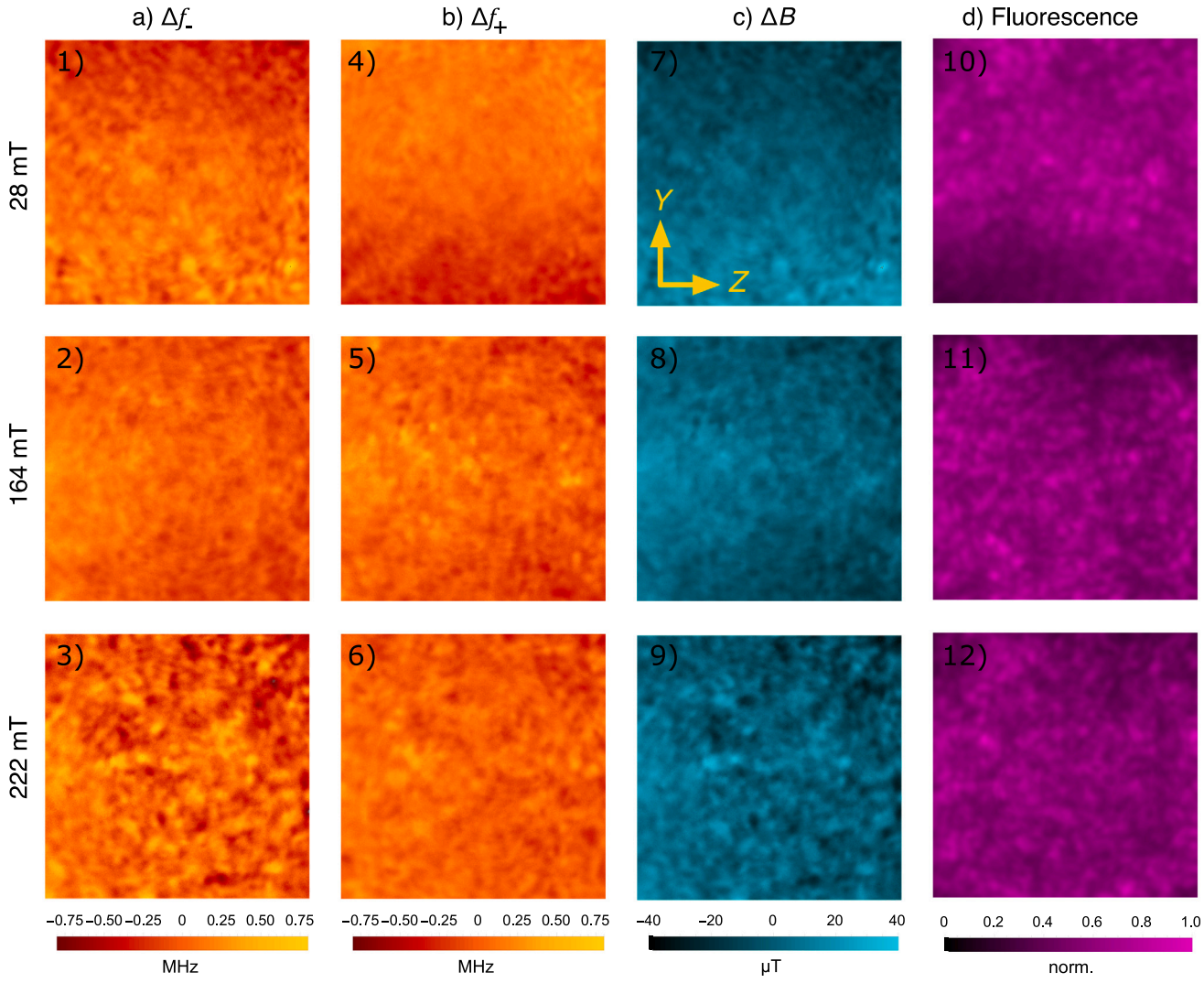

Fig. 6. Top: Magnetic field images at a bias magnetic field of 28 mT. **Middle**: Magnetic field images at a bias magnetic field of 164 mT. **Bottom**: Magnetic field images at a bias magnetic field of 222 mT. From left to right: ODMR frequency shift map obtained from the $|0\rangle \longrightarrow |-1\rangle$ transition, ODMR frequency shift map obtained from the $|0\rangle \longrightarrow |+1\rangle$ transition, magnetic field map obtained using the difference of the frequency shifts from both transitions ($|0\rangle \longrightarrow \pm 1\rangle$) and dividing the difference with the coefficient of 28.03 MHz/mT, the normalized fluorescence map from both of the transitions.

By looking at this color map we can see that even the largest gradient measured with this system ≈1.3 μT/μm or ≈0.65 μT/px at an average FWHM of 6 MHz of an ODMR profile is well within the zone, where the ODMR signal broadening is below 1%.

The central frequencies of the ODMR measurements, corresponding frequency ranges and magnetic field values, and gradient values vary by the applied bias field. The values of these parameters are compiled in Table 1.

Table 1
Results: ODMR frequency variations ($\Delta f_{\pm 1}$) for both $|0\rangle \longrightarrow |+1\rangle$ and $|0\rangle \longrightarrow |-1\rangle$ transitions. Using the results from both of these transitions the variation of the magnetic field over the field of view (ΔB) is also obtained. The gradient values ΔB_Y and ΔB_Z were estimated by dividing the linearly fitted values in Fig. 8 with the corresponding bias magnetic field values.

f_{-1}, MHz	Δf_{-1}, MHz	f_{+1}, MHz	Δf_{+1}, MHz	B, mT	ΔB, μT	ΔB_Y, nT/μm	ΔB_Y, ppm/μm	ΔB_Z, nT/μm	ΔB_Z, ppm/μm
2080	1.45	3659	0.85	28	70	1350	48	3.48	0.12
1740	0.85	7479	1.05	164	56	213	1.3	786	4.8
3354	3.6	9091	1.7	222	170	364	1.6	514	2.3

5. Conclusions

In this study we have given a blueprint for a setup for a compact, tunable and uniform magnetic field source, using cylindrical diametrically magnetized permanent magnets with flux homogenizers that can be used for various microscopy applications that focus on micrometer scale. On one hand this electro-mechanically controllable system not only gives a compact, inexpensive and energy efficient alternative for electromagnets, that is not prone to heating up during usage, and does not rely on the quality of power supplies, but also allows modifications to fit different needs. Moreover, the design presented here at created 222 mT magnetic field gives a magnetic field gradient of 2 ppm/μm or 0.5 μT/μm. In comparison to a magnetic field setup using just one disk magnet, commonly used in similar experiments to generate the bias magnetic field, where the typical obtained magnetic field gradients are about 2–3 μT/μm at magnetic fields of 20–30 mT [12]. On the other

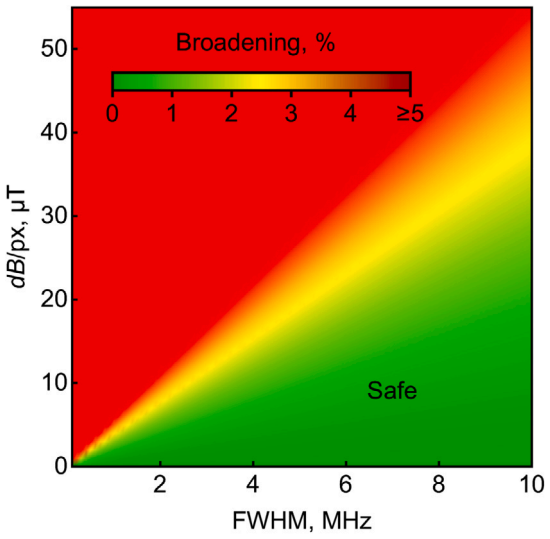

Fig. 7. The broadening of the FWHM of an ODMR profile in relation to the magnetic field gradient over one detection pixel (0.5×0.5 μm^2). The color scale indicates the regions where the broadening is negligible (green) and regions where broadening will have a noticeable effect on the measurement (red).

hand, the presented device is much simpler and easy to customize compared to other permanent magnet-based alternatives, while delivering comparable field homogeneity in micro-scale applications.

Rotation of both of the permanent magnets around their main cylindrical axes allows for rapid changes from a close to zero magnetic field to a relatively high magnetic field, giving a useful tool for hysteresis measurements, usually requiring a combination of relatively large magnetic fields with the possibility to gradually increase or decrease the magnetic field, as well as the ability to change the direction of the magnetic field. Furthermore, this same design potentially allows for measurements requiring a dynamically changing magnetic field (for instance, magnetic relaxation measurements), yet rapid full revolution rotations of the magnet cylinders would cause changing mechanical stresses experienced by the whole setup, that would need to be accounted for.

The maximum magnetic field produced by the system presented in this work (222.1 mT) is mainly limited by the distance between the magnets, the flux homogenizers and the center of the device, and by the magnet properties. The main obstacle in similar setups is the diameter of the microscope objective (in our case 25 mm). One immediate solution could be the usage of long working distance objectives [11], that, on one hand, allow to put the microscope objective outside the volume between the flux homogenizers, but, on the other hand, dramatically reduce the spatial resolution and the light collection efficiency of the system.

The minimum magnetic field that the current experimental setup device was able to produce was ≈0.95 mT. This value agrees well with the 2D magnetic field simulations (Fig. 3(c)). A conclusion that can be drawn from measurements and simulations is that this type of system cannot reliably generate a zero magnetic field unaided, due to stray magnetic fields (the Earth or laboratory) that can easily change the field properties, and even in the best case scenario the zero field region is very narrow. This is not a problem for NV ensemble based measurements, as low magnetic fields cause a degeneration of the energetic levels of the differently oriented NV centers [40], thus making the magnetic field measurements based on ODMR position determination challenging.

The presented magnetic field source design is not limited to NV based measurements, as very similar requirements for a magnetic field source can be found in other methods, like Magneto Optic Kerr Effect (MOKE) measurements [41].

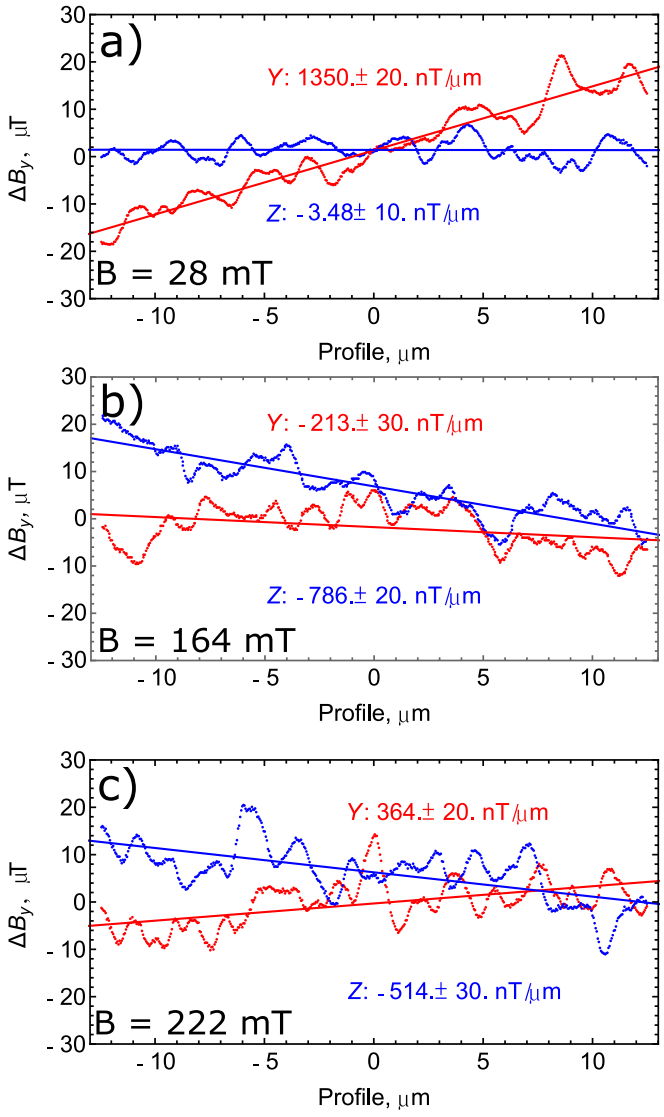

Fig. 8. Experimental results of the magnetic field gradient (with ferrites between the permanent magnets). These line plots representing the magnetic field gradients are constructed in the following way, both profiles Y and Z are constructed by taking data from the middle part of the magnetic field profiles presented in column (c) of Fig. 6. To lessen the impact of the noise we averaged 30 adjacent pixel rows for Z profile, and 30 adjacent columns for Y profile. The straight lines are linear fits of the data, the slope values give the change in magnetic field per μm for each direction.

Declaration of competing interest

The authors declare that they have no known competing financial interests or personal relationships that could have appeared to influence the work reported in this paper.

Acknowledgments

A. Berzins, H. Grube and R. Lazda acknowledges support from Latvian Council of Science project lzp-2020/2-0243 “Robust and fast quantum magnetic microscope with concentrated bias field”. I. Fescenko acknowledges support from ERAF project 1.1.1.5/20/A/001 (Latvia). We also acknowledge LLC “MikroTik” donation projects (Latvia), administered by the UoL foundation: “Improvement of Magnetic field imaging system” for opportunity to significantly improve experimental setup, “Simulations for stimulation of science” for opportunity to acquire COMSOL license, and project “Annealing furnace for the development of new nanometer-sized sensors and devices”.

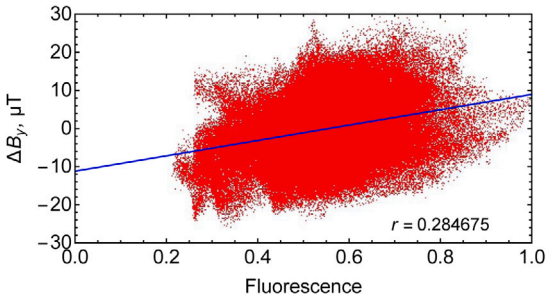

Fig. 9. Magnetic field ΔB_y (Fig. 6(8)) vs. normalized fluorescence (Fig. 6(11)) plotted pixel-wise alongside with a linear fit and Pearson correlation in the inset.

Appendix. Noise structure in the magnetic field maps

As the magnetic field maps contain some noise structure, we tried to find their origin. The plausible causes in our understanding could be: NV layer illumination related artifacts in combination with ODMR profile fitting artifacts, and NV distribution. To analyze the possible NV layer illumination contribution to the noise structure we created a correlation graph for the 164 mT measurement where the magnetic field map (Fig. 6(8)) is correlated with the fluorescence map (Fig. 6(11)), see Fig. 9. As can be seen from this graph, there is some correlation between the fluorescence distribution and the magnetic field distribution, meaning that the fluorescence distribution to some extent impacts the noise in the magnetic field images. This might be connected with ODMR profile fitting related artifacts. As the shape of the ODMR profile at 3000 averages is still a little rough, and part of the noise signal might come from small spatial illumination fluctuations, it is possible that a fit with a single Lorentzian profile could give small deviations in the resonance frequency value. Moreover, if the noise structure is caused by this effect, it is easy to explain the sharp transitions between neighboring regions (pixels) that should have relatively smooth transitions in the case of optical signals coming from the NV fluorescence region (due to diffraction limited spatial resolution). Artifacts due to the NV distribution are not very likely, as in our case the spatial resolution of the system is around 0.7 μm, meaning that if one can see spatial fluctuation in the NV distribution, these fluctuations should be relatively sharp. But taking into account the He ion implantation doses and annealing process it is unlikely.

References

[1] M.N.R. Ashfold, J.P. Goss, B.L. Green, P.W. May, M.E. Newton, C.V. Peaker, Nitrogen in diamond, Chem. Rev. 120 (12) (2020) 5745–5794, URL https://pubs.acs.org/doi/10.1021/acs.chemrev.9b00518, ISSN 0009-2665, 1520-6890.

[2] A. Waxman, Y. Schlussel, D. Groswasser, V.M. Acosta, L.-S. Bouchard, D. Budker, R. Folman, Diamond magnetometry of superconducting thin films, Phys. Rev. B 89 (5) (2014) 054509, URL https://link.aps.org/doi/10.1103/PhysRevB.89.054509, Publisher: American Physical Society.

[3] Y. Xu, Y. Yu, Y.Y. Hui, Y. Su, J. Cheng, H.-C. Chang, Y. Zhang, Y.R. Shen, C. Tian, Mapping dynamical magnetic responses of ultrathin micron-size superconducting films using nitrogen-vacancy centers in diamond, Nano Lett. (ISSN: 1530-6984) 19 (8) (2019) 5697–5702, URL https://doi.org/10.1021/acs.nanolett.9b02298, Publisher: American Chemical Society.

[4] L.M. Pham, D.L. Sage, P.L. Stanwix, T.K. Yeung, D. Glenn, A. Trifonov, P. Cappellaro, P.R. Hemmer, M.D. Lukin, H. Park, A. Yacoby, R.L. Walsworth, Magnetic field imaging with nitrogen-vacancy ensembles, New J. Phys. (ISSN: 1367-2630) 13 (4) (2011) 045021, URL https://doi.org/10.1088/1367-2630/13/4/045021, Publisher: IOP Publishing.

[5] K. Mizuno, H. Ishiwata, Y. Masuyama, T. Iwasaki, M. Hatano, Simultaneous wide-field imaging of phase and magnitude of AC magnetic signal using diamond quantum magnetometry, Sci. Rep. (ISSN: 2045-2322) 10 (1) (2020) 11611, URL https://www.nature.com/articles/s41598-020-68404-5, Number: 1 Publisher: Nature Publishing Group.

[6] A. Horsley, P. Appel, J. Wolters, J. Achard, A. Tallaire, P. Maletinsky, P. Treutlein, Microwave device characterization using a widefield diamond microscope, Phys. Rev. A 10 (4) (2018) 044039, URL https://link.aps.org/doi/10.1103/PhysRevApplied.10.044039, Publisher: American Physical Society.

[7] I. Fescenko, A. Laraoui, J. Smits, N. Mosavian, P. Kehayias, J. Seto, L. Bougas, A. Jarmola, V.M. Acosta, Diamond magnetic microscopy of malarial hemozoin nanocrystals, Phys. Rev. A 11 (3) (2019) 034029, URL https://link.aps.org/doi/10.1103/PhysRevApplied.11.034029, Publisher: American Physical Society.

[8] J. Smits, A. Berzins, F.H. Gahbauer, R. Ferber, K. Erglis, A. Cebers, J. Prikulis, Estimating the magnetic moment of microscopic magnetic sources from their magnetic field distribution in a layer of nitrogen-vacancy (NV) centres in diamond, Eur. Phys. J. Appl. Phys. 73 (2) (2016) 20701, URL https://www.epjap.org/articles/epjap/abs/2016/02/ap150449/ap150449.html, ISSN 1286-0042, 1286-0050.

[9] T. Lenz, G. Chatzidrosos, Z. Wang, L. Bougas, Y. Dumeige, A. Wickenbrock, N. Kerber, J. Zázvorka, F. Kammerbauer, M. Kläui, Z. Kazi, K.-M.C. Fu, K.M. Itoh, H. Watanabe, D. Budker, Imaging topological spin structures using light-polarization and magnetic microscopy, Phys. Rev. A (ISSN: 2331-7019) 15 (2) (2021) 024040, URL https://link.aps.org/doi/10.1103/PhysRevApplied.15.024040.

[10] P. Appel, B.J. Shields, T. Kosub, N. Hedrich, R. Hübner, J. Faßbender, D. Makarov, P. Maletinsky, Nanomagnetism of magnetoelectric granular thin-film antiferromagnets, Nano Lett. (ISSN: 1530-6984) 19 (3) (2019) 1682–1687, URL https://doi.org/10.1021/acs.nanolett.8b04681, Publisher: American Chemical Society.

[11] A. Berzins, J. Smits, A. Petruhins, H. Grube, Surface magnetic structure investigation of a nanolaminated Mn2GaC thin film using a magnetic field microscope based on Nitrogen-Vacancy centers, Mater. Chem. Phys. (ISSN: 02540584) 272 (2021) 124972, URL https://linkinghub.elsevier.com/retrieve/pii/S0254058421007550.

[12] A. Berzins, J. Smits, A. Petruhins, Characterization of microscopic ferromagnetic defects in thin films using magnetic microscope based on Nitrogen-Vacancy centres, Mater. Chem. Phys. (ISSN: 02540584) 267 (2021) 124617, URL https://linkinghub.elsevier.com/retrieve/pii/S0254058421004004.

[13] F. Ziem, M. Garsi, H. Fedder, J. Wrachtrup, Quantitative nanoscale MRI with a wide field of view, Sci. Rep. (ISSN: 2045-2322) 9 (1) (2019) 12166, URL https://www.nature.com/articles/s41598-019-47084-w, Number: 1 Publisher: Nature Publishing Group.

[14] S. Steinert, F. Ziem, L.T. Hall, A. Zappe, M. Schweikert, N. Götz, A. Aird, G. Balasubramanian, L. Hollenberg, J. Wrachtrup, Magnetic spin imaging under ambient conditions with sub-cellular resolution, Nature Commun. (ISSN: 2041-1723) 4 (1) (2013) 1607, URL https://www.nature.com/articles/ncomms2588, Number: 1 Publisher: Nature Publishing Group.

[15] G. Chatzidrosos, A. Wickenbrock, L. Bougas, H. Zheng, O. Tretiak, Y. Yang, D. Budker, Eddy-current imaging with nitrogen-vacancy centers in diamond, Phys. Rev. A (ISSN: 2331-7019) 11 (1) (2019) 014060, URL https://link.aps.org/doi/10.1103/PhysRevApplied.11.014060.

[16] J.-F. Wang, F.-F. Yan, Q. Li, Z.-H. Liu, H. Liu, G.-P. Guo, L.-P. Guo, X. Zhou, J.-M. Cui, J. Wang, Z.-Q. Zhou, X.-Y. Xu, J.-S. Xu, C.-F. Li, G.-C. Guo, Coherent control of nitrogen-vacancy center spins in silicon carbide at room temperature, Phys. Rev. Lett. 124 (22) (2020) 223601, URL https://link.aps.org/doi/10.1103/PhysRevLett.124.223601, Publisher: American Physical Society.

[17] T. Plakhotnik, D. Gruber, Luminescence of nitrogen-vacancy centers in nanodiamonds at temperatures between 300 and 700 K: perspectives on nanothermometry, Phys. Chem. Chem. Phys. (ISSN: 1463-9084) 12 (33) (2010) 9751–9756, URL https://pubs.rsc.org/en/content/articlelanding/2010/cp/c001132k, Publisher: The Royal Society of Chemistry.

[18] X. Zhang, G. Chatzidrosos, Y. Hu, H. Zheng, A. Wickenbrock, A. Jerschow, D. Budker, Battery characterization via eddy-current imaging with nitrogen-vacancy centers in diamond, Appl. Sci. (ISSN: 2076-3417) 11 (7) (2021) 3069, URL https://www.mdpi.com/2076-3417/11/7/3069.

[19] O. Tretiak, P. Blümler, L. Bougas, Variable single-axis magnetic-field generator using permanent magnets, AIP Adv. (ISSN: 2158-3226) 9 (11) (2019) 115312, URL http://aip.scitation.org/doi/10.1063/1.5130896.

[20] P.V. Trevizoli, J.A. Lozano, G.F. Peixer, J.R. Barbosa Jr., Design of nested Halbach cylinder arrays for magnetic refrigeration applications, J. Magn. Magn. Mater. (ISSN: 03048853) 395 (2015) 109–122, URL https://linkinghub.elsevier.com/retrieve/pii/S0304885315303309.

[21] R. Bjrk, A. Smith, C. Bahl, Analysis of the magnetic field, force, and torque for two-dimensional halbach cylinders, J. Magn. Magn. Mater. (ISSN: 03048853) 322 (1) (2010) 133–141, URL https://linkinghub.elsevier.com/retrieve/pii/S0304885309008816.

[22] H.A. Leupold, A.S. Tilak, E. Potenziani, Multi-Tesla permanent magnet field sources, J. Appl. Phys. 73 (10) (1993) 6861–6863, URL http://aip.scitation.org/doi/10.1063/1.352463, ISSN 0021-8979, 1089-7550.

[23] H.A. Leupold, E. Potenziani II, M.G. Abele, Applications of yokeless flux confinement, J. Appl. Phys. 64 (10) (1988) 5994–5996, URL http://aip.scitation.org/doi/10.1063/1.342148, ISSN 0021-8979, 1089-7550.

[24] N. Riahi, A. Komaee, Steering magnetic particles by feedback control of permanent magnet manipulators, in: 2019 American Control Conference (ACC), IEEE, Philadelphia, PA, USA, ISBN: 978-1-5386-7926-5, 2019, pp. 5432–5437, URL https://ieeexplore.ieee.org/document/8815060/.

[25] J. Hilton, S. McMurry, An adjustable linear Halbach array, J. Magn. Magn. Mater. (ISSN: 03048853) 324 (13) (2012) 2051–2056, URL https://linkinghub.elsevier.com/retrieve/pii/S030488531200100X.

[26] G. Moresi, R. Magin, Miniature permanent magnet for table-top NMR, Concepts Magn. Reson. 19B (1) (2003) 35–43, URL https://onlinelibrary.wiley.com/doi/10.1002/cmr.b.10082, ISSN 1043-7347, 1099-0534.

[27] T. Honma, M. Fujioka, T. Shinozuka, N. Matsumoto, A permanent-magnet dipole with variable field strength and polarity, Nucl. Instrum. Methods Phys. Res. A (ISSN: 01689002) 361 (1–2) (1995) 13–20, URL https://linkinghub.elsevier.com/retrieve/pii/0168900295001433.

[28] O. Cugat, P. Hansson, J. Coey, Permanent magnet variable flux sources, IEEE Trans. Magn. (ISSN: 00189464) 30 (6) (1994) 4602–4604, URL http://ieeexplore.ieee.org/document/334162/.

[29] M.C. Tayler, D. Sakellariou, Low-cost, pseudo-Halbach dipole magnets for NMR, J. Magn. Reson. (ISSN: 10907807) 277 (2017) 143–148, URL https://linkinghub.elsevier.com/retrieve/pii/S1090780717300630.

[30] Q. Peng, S. McMurry, J. Coey, Cylindrical permanent-magnet structures using images in an iron shield, IEEE Trans. Magn. (ISSN: 0018-9464) 39 (4) (2003) 1983–1989, URL http://ieeexplore.ieee.org/document/1211170/.

[31] D. Barlow, R. Kraus, R. Meyer, Variable-field permanent-magnet dipole, IEEE Trans. Magn. 30 (4) (1994) 2285–2287, URL http://ieeexplore.ieee.org/document/305731/, ISSN 0018-9464, 1941-0069.

[32] Q.-C. Sun, T. Song, E. Anderson, A. Brunner, J. Förster, T. Shalomayeva, T. Taniguchi, K. Watanabe, J. Gräfe, R. Stöhr, X. Xu, J. Wrachtrup, Magnetic domains and domain wall pinning in atomically thin CrBr3 revealed by nanoscale imaging, Nature Commun. (ISSN: 2041-1723) 12 (1) (2021) 1989, URL http://www.nature.com/articles/s41467-021-22239-4.

[33] B.J. Maertz, A.P. Wijnheijmer, G.D. Fuchs, M.E. Nowakowski, D.D. Awschalom, Vector magnetic field microscopy using nitrogen vacancy centers in diamond, Appl. Phys. Lett. 96 (9) (2010) 092504, URL http://aip.scitation.org/doi/10.1063/1.3337096, ISSN 0003-6951, 1077-3118.

[34] X. Gu, Flat-cladding fiber bragg grating sensors for large strain amplitude fatigue tests, in: Opto-Mechanical Fiber Optic Sensors, Elsevier, ISBN: 978-0-12-803131-5, 2018, pp. 49–73, URL https://linkinghub.elsevier.com/retrieve/pii/B9780128031315000039.

[35] G.A. Paterson, X. Zhao, M. Jackson, D. Heslop, Measuring, processing, and analyzing hysteresis data, Geochem. Geophys. Geosyst. 19 (7) (2018) 1925–1945, URL https://onlinelibrary.wiley.com/doi/10.1029/2018GC007620, ISSN 1525-2027, 1525-2027.

[36] L. Rondin, J.-P. Tetienne, T. Hingant, J.-F. Roch, P. Maletinsky, V. Jacques, Magnetometry with nitrogen-vacancy defects in diamond, Rep. Progr. Phys. 77 (5) (2014) 056503, URL https://iopscience.iop.org/article/10.1088/0034-4885/77/5/056503, ISSN 0034-4885, 1361-6633.

[37] J.F. Ziegler, M.D. Ziegler, J.P. Biersack, SRIM – the stopping and range of ions in matter (2010), Nucl. Instrum. Methods Phys. Res. B (ISSN: 0168-583X) 268 (11) (2010) 1818–1823, URL http://www.sciencedirect.com/science/article/pii/S0168583X10001862.

[38] I. Fescenko, A. Jarmola, I. Savukov, P. Kehayias, J. Smits, J. Damron, N. Ristoff, N. Mosavian, V.M. Acosta, Diamond magnetometer enhanced by ferrite flux concentrators, Phys. Rev. Res. (ISSN: 2643-1564) 2 (2) (2020) 023394, URL https://link.aps.org/doi/10.1103/PhysRevResearch.2.023394.

[39] M. Auzinsh, A. Berzins, D. Budker, L. Busaite, R. Ferber, F. Gahbauer, R. Lazda, A. Wickenbrock, H. Zheng, Hyperfine level structure in nitrogen-vacancy centers near the ground-state level anticrossing, Phys. Rev. B 100 (7) (2019) 075204, URL https://link.aps.org/doi/10.1103/PhysRevB.100.075204, Publisher: American Physical Society.

[40] T. Mittiga, S. Hsieh, C. Zu, B. Kobrin, F. Machado, P. Bhattacharyya, N. Rui, A. Jarmola, S. Choi, D. Budker, N. Yao, Imaging the local charge environment of nitrogen-vacancy centers in diamond, Phys. Rev. Lett. 121 (24) (2018) 246402, URL https://link.aps.org/doi/10.1103/PhysRevLett.121.246402, ISSN 0031-9007, 1079-7114.

[41] D. Kim, Y.-W. Oh, J.U. Kim, S. Lee, A. Baucour, J. Shin, K.-J. Kim, B.-G. Park, M.-K. Seo, Extreme anti-reflection enhanced magneto-optic Kerr effect microscopy, Nature Commun. (ISSN: 2041-1723) 11 (1) (2020) 5937, URL http://www.nature.com/articles/s41467-020-19724-7.